

REVIEW ARTICLE

The Quantum Lattice Boltzmann Equation: Recent Developments[†]

Silvia Palpacelli^{1,*} and Sauro Succi²

¹ *Dipartimento di Matematica, Università Roma Tre, Largo San Leonardo Murialdo 1, 00146, Roma, Italy.*

² *Istituto Applicazioni del Calcolo, Viale Policlinico 137, 00161 Roma, Italy.*

Received 26 February 2008; Accepted (in revised version) 25 June 2008

Available online 8 July 2008

Abstract. The derivation of the quantum lattice Boltzmann model is reviewed with special emphasis on recent developments of the model, namely, the extension to a multi-dimensional formulation and the application to the computation of the ground state of the Gross-Pitaevskii equation (GPE). Numerical results for the linear and non-linear Schrödinger equation and for the ground state solution of the GPE are also presented and validated against analytical results or other classical schemes such as Crank-Nicholson.

PACS: 02.70.-c, 03.65-w, 03.67.Lx

Key words: Quantum lattice Boltzmann, multi-dimensions, imaginary-time model, linear and non-linear Schrödinger equation, adiabatic limit.

Contents

1	Introduction	981
2	Formal parallel between LBE and Dirac equation	982
3	Quantum lattice Boltzmann equation	985
4	One-dimensional quantum lattice Boltzmann model	986
5	Extension to two and three spatial dimensions	987
6	Adding a potential to the qLB model	989
7	Imaginary-time quantum lattice Boltzmann model	990

[†]Dedicated to Professor Xiantu He on the occasion of his 70th birthday.

*Corresponding author. *Email addresses:* palpacel@mat.uniroma3.it (S. Palpacelli), succi@iac.rm.cnr.it (S. Succi)

8	Numerical results	993
9	Conclusions and outlook	1005

1 Introduction

Lattice Boltzmann models (LBMs) have become a competitive numerical tool for simulating fluid flows over a wide range of complex physical problems [1–7]. LBMs were initially derived from lattice gas cellular automata (LGCA). The basic idea of LGCA is to simulate the macroscopic behavior of a fluid flow by implementing an extremely simplified model of the microscopic interactions between particles. LBMs were developed, starting from LGCA, in the attempt to overcome their major drawbacks: statistical noise, increasing complexity of the collision operator (for three dimensional problems) and high viscosity (due to small number of collisions) [1–3]. Nowadays, LBM has consolidated into a powerful alternative to more classical computational fluid dynamics models based on the discretization of the Navier-Stokes equations of continuum mechanics.

However, LBM and, in general, the lattice kinetic approach has been mostly used with classical (non-quantum) fluid. Nonetheless, with the theorization of quantum computers, some authors have extended the lattice kinetic approach to quantum mechanics [8–16]. In fact, as it was first suggested by Feynman [17], the most natural application of quantum computers would be quantum mechanics [18]. The lattice kinetic approach is very interesting in this respect, because it was shown that the so-called quantum lattice gas cellular automata (QLGCA) [11] can be used to simulate systems of nonrelativistic quantum particles with exponential speedup in the number of particles [8].

Besides their hypothetical and future application to quantum computing, these lattice kinetic methods for quantum mechanics are interesting numerical schemes, which can be implemented on classical computers retaining the usual attractive features of LGCA and LBM: simplicity, computational speed, straightforward parallel implementation.

In this paper, we will focus on the so-called quantum lattice Boltzmann (qLB) model proposed by Succi and Benzi [16, 19]. The qLB model was initially derived from a formal parallel between the kinetic lattice Boltzmann equation (LBE) and the relativistic Dirac equation. It was then shown that the non-relativistic Schrödinger equation ensues from the Dirac equation under an adiabatic assumption that is formally similar to the one which takes the Boltzmann equation to the Navier-Stokes equations in kinetic theory [16].

The basic idea of the qLB model is to associate the wave functions composing the Dirac quadrispinor with the discrete distribution functions of the LBE. In one spatial dimension, this analogy is natural and the quadrispinor components can be assimilated to quantum particles of different types propagating with velocities $\pm c$ and colliding when they meet at the same space-time location. However, in multi-dimensional formulation, the analogy is no longer straightforward. This is mainly due to the fact that the Dirac streaming operator is not diagonal along all the spatial directions (i.e., Dirac matrices can not be simultaneously diagonalized). We could roughly say that, unlike classical

particles, quantum particles of different types mix up while propagating (“spinning particles”). To cope with this problem, a new step has to be included besides the classical collision and streaming steps: a so-called “rotation” step. The rotation step is needed to align the spin along each direction of propagation [16].

Recently, such multi-dimensional version of the model has been implemented and numerically validated [20]. Moreover, an imaginary-time version of the model has been proposed to compute the ground state solution of the Gross-Pitaevskii equation (GPE) [21]. In this paper, we will review the theoretical derivation of the qLB model and its most recent developments and applications. Numerical results for the two-dimensional linear Schrödinger equation, one- and two-dimensional nonlinear Schrödinger equation (namely the GPE) and for the ground state solution of the GPE are also presented.

2 Formal parallel between LBE and Dirac equation

The quantum lattice Boltzmann equation (qLBE) was initially derived from a formal parallel between the kinetic lattice Boltzmann equation and the Dirac equation [16, 22]. This association was suggested by the interesting analogies between quantum mechanics and fluid mechanics which were pointed out from the early days of the formulation of quantum theory [23]. For example, it is well known that the non-relativistic Schrödinger equation can be written in fluid form by simply defining the quantum fluid density and momentum as $\rho = |\psi|^2$ and $J_a \equiv \rho u_a = (\hbar/m)\rho\partial_a\theta$, where the complex wave function ψ is represented as $\psi = \rho^{1/2}\exp(i\theta)$. A similar analogy is also valid for the relativistic Dirac equation. In this case, the quantum fluid can be seen as a mixture of particles of four different types, since the Dirac equation describes the time evolution of a complex quadrispinor $\psi = (\psi_1, \psi_2, \psi_3, \psi_4)^T$. As for classical particle motion, these quantum particles propagate in space and collide when they “meet”, but, differently from classical particles, they get mixed during the streaming step because the Dirac streaming operator is not diagonal [22].

For all their intellectual charm, it is now commonly accepted that they are only formal similarities. However, they can be extremely useful for modeling purposes to formulate non-relativistic quantum mechanics in terms of first-order (relativistic) numerical schemes. As we mentioned, the qLBE is based on an analogy between the LBE and the Dirac equation. To clarify this point, we consider the kinetic LBE

$$f_i(\mathbf{x} + \mathbf{v}_i\Delta t, t + \Delta t) - f_i(\mathbf{x}, t) = A_{ij}(f_j - f_j^{eq}), \quad (2.1)$$

where f_i for $i=1, \dots, b$ are the discrete distribution functions along the lattice speeds \mathbf{v}_i , f_i^{eq} are the equilibrium distribution functions and A_{ij} is the scattering matrix. This equation can be thought of as a discretization of the following set of partial differential equations:

$$\partial_t f_i + v_{ia}\partial_a f_i = A_{ij}(f_j - f_j^{eq}). \quad (2.2)$$

It can be shown that Eq. (2.2) is the first-order equation resulting from the multiscale expansion procedure commonly adopted to study the macrodynamics of LBE [4]. Eq. (2.2) is formally very similar to the Dirac equation

$$\partial_t \psi_i + c \alpha_{ij}^a \partial_a \psi_j = i \frac{mc^2}{\hbar} \beta_{ij} \psi_j, \quad (2.3)$$

where α^a for $a = x, y, z$ and β are the standard Dirac matrices, c is the speed of light and m is the mass of the particle.

By projecting Eq. (2.2) upon the eigenvectors of the scattering matrix A_{ij} , a set of hyperbolic equations for the hydrodynamic fields

$$\rho = \sum_i f_i, \quad \rho u_a = \sum_i v_{ia} f_i, \quad P_{ab} = \sum_i v_{ia} v_{ib} f_i$$

are derived. From LBE theory, it is known that Navier-Stokes equations ensue from the hyperbolic system deriving from Eq. (2.2) by means of an adiabatic assumption. In this context, adiabatic assumption means that the shear tensor $S_{ab} = \sum_i Q_{iab} f_i$ (with $Q_{iab} = v_{ia} v_{ib} - (v^2/D) \delta_{ab}$, where v is the norm of the lattice vectors v_i and D is the number of spatial dimensions) is adiabatically enslaved to its equilibrium value in the low Knudsen number limit:

$$|\partial_t S_{ab}| \ll \lambda (S_{ab} - S_{ab}^{eq}),$$

where λ is the leading eigenvalue of the scattering matrix A_{ij} [4].

The Schrödinger equation can be derived from the Dirac equation in a formally equivalent adiabatic assumption valid in the non-relativistic limit $\beta = v/c \ll 1$, where v is the particle speed. To show this point, we consider, for the sake of simplicity, the one dimensional version of Eq. (2.3) written in the Majorana form [24], where all the streaming matrices are real valued. This reads:

$$\begin{aligned} \partial_t u_{1,2} + c \partial_z u_{1,2} &= \omega_c d_{2,1}, \\ \partial_t d_{1,2} - c \partial_z d_{1,2} &= -\omega_c u_{2,1}, \end{aligned} \quad (2.4)$$

where $u_{1,2}$ and $d_{1,2}$ are the four wave functions composing the Dirac quadrispinor and $\omega_c = mc^2/\hbar$ is the Compton frequency. Let us define the symmetric/antisymmetric modes according to the unitary transformation

$$\phi_{1,2}^\pm = \frac{1}{\sqrt{2}} (u_{1,2} \pm i d_{2,1}).$$

Starting from Eq. (2.4), it is easy to check that $\phi_{1,2}^\pm$ fulfill the following equations:

$$\begin{aligned} \partial_t \phi_{1,2}^+ + c \partial_z \phi_{1,2}^- &= -i \omega_c \phi_{1,2}^+, \\ \partial_t \phi_{1,2}^- + c \partial_z \phi_{1,2}^+ &= i \omega_c \phi_{1,2}^-. \end{aligned} \quad (2.5)$$

Up to now, the system is still symmetric and time and space derivative are in balance (both first order). As in kinetic theory, we need to break the symmetry of this hyperbolic system and write it in a dissipative form, where spatial and time derivative are no more in balance. The symmetry is broken by choosing a specific time direction via the energy phase-shift $\phi_{1,2}^{\pm} \rightarrow \phi_{1,2}^{\pm} \exp(i\omega_c t)$ [25]. With this definition of $\phi_{1,2}^{\pm}$, Eq. (2.5) transform into:

$$\begin{aligned}\partial_t \phi_{1,2}^+ + c \partial_z \phi_{1,2}^- &= 0, \\ \partial_t \phi_{1,2}^- + c \partial_z \phi_{1,2}^+ &= 2i\omega_c \phi_{1,2}^-.\end{aligned}\quad (2.6)$$

In the non-relativistic limit, $\beta = v/c \ll 1$, the following adiabatic assumption holds:

$$|\partial_t \phi_{1,2}^-| \ll 2\omega_c |\phi_{1,2}^-|.$$

From the second equation of Eq. (2.6), by neglecting the time derivative, we obtain

$$\phi_{1,2}^- \sim \frac{c}{2i\omega_c} \partial_z \phi_{1,2}^+.\quad (2.7)$$

Inserting Eq. (2.7) into the first equation of Eq. (2.6), we finally obtain the Schrödinger equation for a free particle of mass m ,

$$i\hbar \partial_t \phi_{1,2}^+ = -\frac{\hbar^2}{2m} \partial_z^2 \phi_{1,2}^+.$$

The fast modes $\phi_{1,2}^-$ can be thought of as “ghost” variables of the dynamics, in the sense that they are needed to preserve the correct symmetries, although they do not “emerge” at the macroscopic scale. To inspect the behavior of $\phi_{1,2}^-$ with respect to $\phi_{1,2}^+$, we rewrite Eq. (2.5) in terms of the energy and momentum operators of quantum mechanics $i\hbar \partial_t \rightarrow E$, $-i\hbar \partial_z \rightarrow p_z$:

$$\begin{aligned}E \phi_{1,2}^+ - c p_z \phi_{1,2}^- &= mc^2 \phi_{1,2}^+, \\ E \phi_{1,2}^- - c p_z \phi_{1,2}^+ &= -mc^2 \phi_{1,2}^-.\end{aligned}\quad (2.8)$$

In order to take the non-relativistic limit, we make the usual replacement $E \rightarrow E' + mc^2$ with $E' \ll mc^2$ for $\beta \rightarrow 0$ [26]. This corresponds to the energy shift and the adiabatic assumption. Hence, Eq. (2.8) becomes

$$\begin{aligned}E' \phi_{1,2}^+ - c p_z \phi_{1,2}^- &= 0, \\ (E' + 2mc^2) \phi_{1,2}^- - c p_z \phi_{1,2}^+ &\sim 2mc^2 \phi_{1,2}^- - c p_z \phi_{1,2}^+ = 0.\end{aligned}\quad (2.9)$$

From the second of Eq. (2.9), we obtain

$$\frac{|\phi_{1,2}^-|}{|\phi_{1,2}^+|} = \frac{1}{2} \frac{v}{c} = \frac{\beta}{2}.$$

From a standard Fourier analysis of Eq. (2.6), i.e., taking

$$\phi^+ = \rho^+ \exp[i(kz - \omega_+ t)], \quad \phi^- = \rho^- \exp[i(kz - \omega_- t)],$$

it can be checked that $\omega_- / \omega_+ \sim 1/\beta^2$. Hence, the amplitude of $\phi_{1,2}^-$ goes to zero for $\beta \rightarrow 0$, while their frequencies increase as $1/\beta^2$. In conclusion, $\phi_{1,2}^-$ are small-amplitude, fast-oscillating wave functions. These ghost fields are similar to the ghost fields emerging from the hydrodynamic LBE. However, there is a fundamental difference: ghost fields for hydrodynamic LBE tend to die out in a short time because of the real valued relaxation coefficient, while $\phi_{1,2}^-$ keep oscillating since their relaxation coefficient is purely imaginary (time-reversible dynamics).

3 Quantum lattice Boltzmann equation

In the previous section, we pointed out an intriguing analogy between the Dirac equation and the LBE: the Schrödinger equation can be obtained from the Dirac equation in the same way as the Navier-Stokes equations is derived from the LBE. This invites a quantitative correspondence between LBE and Dirac equation. To this end, let us consider the three-dimensional Dirac equation in Majorana form. This reads:

$$(\partial_t - c\alpha^x \partial_x + c\beta \partial_y - c\alpha^z \partial_z) \boldsymbol{\psi} = -i\omega_c \alpha^y \boldsymbol{\psi}. \quad (3.1)$$

The formal parallel between Eq. (3.1) and Eq. (2.2) is as follows [16]:

- $f_i \rightarrow \psi_i$,
- $v_i \rightarrow \mathbf{L} \equiv c(-\alpha^x, \beta, -\alpha^z)$,
- $A_{ij} \rightarrow -i\omega_c \alpha_{ij}^y$.

Some observations are in order:

1. the distribution functions f_i are real valued, whereas ψ_i are complex wave functions;
2. the number of distribution functions f_i is related to the lattice used to discretize the phase space, whereas $\boldsymbol{\psi}$ is composed by exactly four complex wave functions independently from the lattice;
3. the LBE streaming operator is diagonal along all the spatial directions, while the Dirac streaming operator is not, because it is not possible to simultaneously diagonalize the matrices $\mathbf{L} = c(-\alpha^x, \beta, -\alpha^z)$.

The main problem of this approach is clearly given by point three above. However, there is a way out: to diagonalize each matrix of \mathbf{L} separately in a sequence. The basic idea is to use an operator splitting technique and hence consider three equivalent formulations of the same equation, each having a diagonal streaming operator along x , y and z , respectively. In practice, we write the one-dimensional Dirac equation with, say, the

z -streaming operator in diagonal form. As we shall see, in this one-dimensional formulation, a full correspondence with LBE is achieved. Thus, collision and streaming are performed along z by using the one-dimensional qLBE. Then the system is rotated (i.e. a unitary transformation Y is applied) so that the y -streaming matrix is diagonal and the qLBE is used along y . Finally, the equation is transformed again so that the x -streaming matrix is diagonal and the qLBE is applied once again. After the three sequential applications of the qLBE, the Dirac quadrispinor is transformed back.

It is evident, from the sketch of this procedure, that the model is built upon the one dimensional version of Eq. (3.1). Hence, in the following section we revise the one-dimensional version of the model.

4 One-dimensional quantum lattice Boltzmann model

Let us consider Eq. (2.4), the one-dimensional Dirac equation in Majorana form. As observed in [16], this is a discrete Boltzmann equation for a couple of complex bispinor $u_{1,2}$ and $d_{1,2}$. The propagation step consists on streaming $u_{1,2}$ and $d_{1,2}$ along z with speeds $\pm c$, respectively, while the collision step is performed according to the scattering matrix of the right hand side of Eq. (2.4).

The quantum lattice Boltzmann (qLB) model is obtained by integrating Eq. (2.4) along the characteristics of $u_{1,2}$ and $d_{1,2}$ respectively and approximating the right hand side integral by using the trapezoidal rule. By assuming $\Delta z = c\Delta t$ (light-cone rule), we have

$$\begin{aligned}\hat{u}_{1,2} - u_{1,2} &= \frac{\tilde{m}}{2}(d_{2,1} + \hat{d}_{2,1}), \\ \hat{d}_{1,2} - d_{1,2} &= -\frac{\tilde{m}}{2}(u_{2,1} + \hat{u}_{2,1}),\end{aligned}\tag{4.1}$$

where $\hat{u}_{1,2} = u_{1,2}(z + \Delta z, t + \Delta t)$, $\hat{d}_{1,2} = d_{1,2}(z - \Delta z, t + \Delta t)$, $u_{1,2} = u_{1,2}(z, t)$, $d_{1,2} = d_{1,2}(z, t)$ and $\tilde{m} = \omega_c \Delta t$ is the lattice Compton frequency. Note that, in the scheme of Eq. (4.1), the integration of the lhs is exact, a numerical error is introduced only by the discretization of the rhs integral. The system of Eq. (4.1) can be algebraically solved for $\hat{u}_{1,2}$ and $\hat{d}_{1,2}$ yielding the qLB scheme in explicit form

$$\begin{aligned}\hat{u}_{1,2} &= au_{1,2} + bd_{2,1}, \\ \hat{d}_{1,2} &= ad_{1,2} - bu_{2,1},\end{aligned}\tag{4.2}$$

where

$$a = \frac{1 - \tilde{m}^2/4}{1 + \tilde{m}^2/4}, \quad b = \frac{\tilde{m}}{1 + \tilde{m}^2/4}.\tag{4.3}$$

The scheme of Eq. (4.2) is a lattice Boltzmann equation in matrix form [3], where the

collision step is performed by applying the unitary collision matrix

$$Q = \begin{pmatrix} a & 0 & 0 & b \\ 0 & a & b & 0 \\ 0 & -b & a & 0 \\ -b & 0 & 0 & a \end{pmatrix}. \quad (4.4)$$

Note that, due to unitarity of the collision matrix Q , the qLB method offers unconditioned stability with the size of the time step/mesh spacing (making sure that the light-cone relation is fulfilled). However, its accuracy is subjected to the condition $\omega_c \Delta t = \Delta z / \lambda_B \leq 1$, where $\lambda_B = c / \omega_c$ is the De Broglie wavelength of the particle. Since the time step scales linearly with the mesh spacing, the grid resolution can be increased without suffering the time step collapse typical of classical explicit schemes where the CFL stability condition, $\Delta t < (2m/\hbar)\Delta z^2$, holds. On the other hand, a lack of adiabaticity could occur for $\omega_c \Delta t \ll 1$, and this effect must be carefully watched, while decreasing the lattice spacing, in order to preserve the validity of qLB.

5 Extension to two and three spatial dimensions

As we mentioned in Section 3, the extension to two and three spatial dimensions requires the introduction of a “rotation” step, besides the usual collision and propagation steps. This is due to the fact that we split the streaming operator and apply three times the one-dimensional qLB model. In particular, assume we start from a formulation of Eq. (3.1), for which the z -streaming matrix is diagonal, and we apply the 1D-qLB scheme along z :

$$\boldsymbol{\psi}(P_z, t + \Delta t) = S_z \tilde{Q} \boldsymbol{\psi}(P, t),$$

where $P = (x, y, z)$, $P_z = P + \Delta z \hat{k}$, S_z is the z -streaming operator and \tilde{Q} is the collision matrix (as we shall see, the collision matrix is not exactly equal to Q of Eq. (4.4), this is due to a factor $1/D$ emerging from the operator splitting procedure). Now, we rotate the system so that it is aligned along y , and we apply, to the transformed equation, the 1D-qLB scheme along y :

$$\boldsymbol{\psi}_y(P_{yz}, t + \Delta t) = S_y \tilde{Q}^y \boldsymbol{\psi}(P_z, t + \Delta t), \quad \text{with} \quad \boldsymbol{\psi}_y = Y \boldsymbol{\psi}, \quad \tilde{Q}^y = Y^{-1} \tilde{Q} Y,$$

where $P_{yz} = P + \Delta y \hat{j} + \Delta z \hat{k}$, S_y is the streaming operator along y . The system is rotated again so that it is aligned along x and the 1D-qLB is applied for the last time:

$$\boldsymbol{\psi}_{xy}(P_{xyz}, t + \Delta t) = S_x \tilde{Q}^{xy} \boldsymbol{\psi}_y(P_{yz}, t + \Delta t), \quad \text{with} \quad \boldsymbol{\psi}_{xy} = X \boldsymbol{\psi}_y, \quad \tilde{Q}^{xy} = X^{-1} \tilde{Q}^y X,$$

where $P_{xyz} = P + \Delta x \hat{i} + \Delta y \hat{j} + \Delta z \hat{k}$, S_x is the streaming operator along x . Finally, the updated value is transformed back $\boldsymbol{\psi} = Y^{-1} X^{-1} \boldsymbol{\psi}_{xy}$.

In the following, we discuss the mathematical details of this procedure in two dimensions, for the three-dimensional case we refer to the original reference [20], however the extension is straightforward.

The starting point is the two-dimensional version of Eq. (3.1)

$$(\partial_t + c\beta\partial_y - c\alpha^z\partial_z)\psi = -i\omega_c\alpha^y\psi,$$

we apply to this equation the unitary transformation Z

$$Z = \frac{1}{\sqrt{2}} \begin{pmatrix} 0 & -1 & 0 & 1 \\ 1 & 0 & -1 & 0 \\ 0 & 1 & 0 & 1 \\ 1 & 0 & 1 & 0 \end{pmatrix},$$

so that the z -streaming matrix operator becomes diagonal. We, thus, obtain the following equivalent problem

$$\begin{cases} (\partial_t + cA^z\partial_z + cA^y\partial_y)\psi = \omega_c C\psi \\ \psi(z,y,0) = \psi_0(z,y), \end{cases} \tag{5.1}$$

where

$$A^z = \begin{pmatrix} 1 & 0 & 0 & 0 \\ 0 & 1 & 0 & 0 \\ 0 & 0 & -1 & 0 \\ 0 & 0 & 0 & -1 \end{pmatrix}, \quad A^y = \begin{pmatrix} 0 & 0 & -1 & 0 \\ 0 & 0 & 0 & -1 \\ -1 & 0 & 0 & 0 \\ 0 & -1 & 0 & 0 \end{pmatrix}, \quad C = \begin{pmatrix} 0 & 0 & 0 & 1 \\ 0 & 0 & 1 & 0 \\ 0 & -1 & 0 & 0 \\ -1 & 0 & 0 & 0 \end{pmatrix}.$$

By using the sequential splitting approach, Eq. (5.1) separates into two one-dimensional problems

$$\begin{cases} (\partial_t + cA^z\partial_z)\psi_1^n = \frac{\omega_c}{2}C\psi_1^n, & (n-1)\Delta t < t \leq \Delta t, \\ \psi_1^n[(n-1)\Delta t] = \psi_2^{n-1}[(n-1)\Delta t], \end{cases} \tag{5.2}$$

and

$$\begin{cases} (\partial_t + cA^y\partial_y)\psi_2^n = \frac{\omega_c}{2}C\psi_2^n, & (n-1)\Delta t < t \leq \Delta t \\ \psi_2^n[(n-1)\Delta t] = \psi_1^n(n\Delta t), \end{cases} \tag{5.3}$$

for $n = 1, 2, \dots, N$. To start the procedure, we set $\psi_2^0 = \psi_0$. The one dimensional problems of Eqs. (5.2) and (5.3) can now be solved by using the 1D-qLB scheme. However, while A^z is already in diagonal form so that the 1D-qLB scheme can be directly applied, the same is not true for A^y . Hence, Eq. (5.3) must be transformed (rotation step) in order to diagonalize A^y and one possible choice for the transformation matrix Y is

$$Y = \frac{1}{\sqrt{2}} \begin{pmatrix} -1 & 0 & 0 & 1 \\ 0 & -1 & 1 & 0 \\ 1 & 0 & 0 & 1 \\ 0 & 1 & 1 & 0 \end{pmatrix}.$$

Note that, the collision matrix of this 2D-qLB is not given by Eq. (4.4), because of the factor 1/2 in the collision term of Eqs. (5.2) and (5.3). By direct calculations, it can be easily shown that, in this case, the collision matrix is obtained from Eq. (4.4) by simply substituting \tilde{m} with $\tilde{m}/2$ in the definition of a and b (see Eq. (4.3)).

6 Adding a potential to the qLB model

In this section, we will show how to add a potential interaction into the model. We will explicitly refer to the one dimensional case for the sake of simplicity. However, the extension to multi-dimensional case is straightforward.

Consider the one-dimensional Dirac equation with an electrostatic potential interaction

$$\begin{aligned}\partial_t u_{1,2} + c \partial_z u_{1,2} &= \omega_c d_{2,1} + i g u_{1,2}, \\ \partial_t d_{1,2} - c \partial_z d_{1,2} &= -\omega_c u_{2,1} + i g d_{1,2},\end{aligned}\quad (6.1)$$

where $g = qV/\hbar$ is the space dependent frequency coupling to the external potential V and q is the particle electric charge. Discretizing as in the free particle case, we obtain

$$\begin{aligned}\hat{u}_{1,2} &= a_g u_{1,2} + b_g d_{2,1}, \\ \hat{d}_{1,2} &= a_g d_{1,2} - b_g u_{2,1},\end{aligned}\quad (6.2)$$

where

$$a_g = \frac{1 - \Omega/4}{1 + \Omega/4 - i\tilde{g}}, \quad b_g = \frac{\tilde{m}}{1 + \Omega/4 - i\tilde{g}},$$

with $\Omega = \tilde{m}^2 - \tilde{g}^2$ and $\tilde{g} = g\Delta t$. We note that, when adding a potential, the Schrödinger equation is still obtained in the adiabatic limit $|\omega - \omega_c| \leq |\omega_c + g|$ but with the additional constraint of "small" potential interaction $|g| \ll \omega_c$. In fact, by following the same procedure outlined in Section 2 to recover the Schrödinger equation from Dirac equation, we obtain

$$\begin{aligned}i\hbar \partial_t \phi_{1,2}^+ &= -\frac{\hbar c^2}{2\omega_c} \partial_z \left(\frac{2\omega_c}{2\omega_c + g} \partial_z \phi_{1,2}^+ \right) - qV \phi_{1,2}^+ \\ &\approx -\frac{\hbar^2}{2m} \partial_z^2 \phi_{1,2}^+ - qV \phi_{1,2}^+, \end{aligned}$$

where the latter approximation is valid only if the potential g is negligible with respect to ω_c .

6.1 The time-dependent Gross-Pitaevskii equation

It is straightforward to apply the scheme of Eq. (6.2) to the solution of the Gross-Pitaevskii equation (GPE), where a nonlinear self-interaction of the wave function is involved [27].

At zero temperature, the dynamics of a trapped Bose-Einstein condensate (BEC) is described by the GPE [28]. The GPE for a quantum wave function $\psi(\mathbf{r}, t)$ with $\mathbf{r} = (x, y, z)^T \in \mathbb{R}^3$ reads as

$$i\hbar \frac{\partial \psi(\mathbf{r}, t)}{\partial t} = \left(-\frac{\hbar^2}{2m} \Delta_{\mathbf{r}} + V_{\text{ext}}(\mathbf{r}) + NU_0 |\psi(\mathbf{r}, t)|^2 \right) \psi(\mathbf{r}, t),$$

where $U_0 = 4\pi\hbar^2 a/m$ is the coupling strength, a is the scattering length and N is the number of particles in the condensate, $V_{\text{ext}}(\mathbf{r})$ is the external trapping potential, usually an harmonic potential. Furthermore, the wave function $\psi(\mathbf{r}, t)$ satisfies the normalization condition

$$\int_{\mathbb{R}^3} |\psi(\mathbf{r}, t)|^2 d\mathbf{r} = 1. \quad (6.3)$$

The three-dimensional GPE can be reduced to two dimensions or even one dimension, still maintaining the same form, for two particular choices of the harmonic trap [29–32]. Hence, in general, we consider the equation

$$i\hbar \frac{\partial \psi(\mathbf{r}, t)}{\partial t} = \left(-\frac{\hbar^2}{2m} \Delta_{\mathbf{r}} + V_{\text{ext}}(\mathbf{r}) + NU_d |\psi(\mathbf{r}, t)|^2 \right) \psi(\mathbf{r}, t), \quad (6.4)$$

for $\mathbf{r} \in \mathbb{R}^d$ with $d = 1, 2, 3$.

To apply the qLB model to this equation, we simply need to define the following total potential

$$V(\mathbf{r}, t) = V_{\text{ext}}(\mathbf{r}) + NU_d |\phi^+|^2,$$

where $|\phi^+|^2 \equiv |\phi_1^+|^2 + |\phi_2^+|^2$. Adding this potential to the model, as shown in the previous section, the slow modes $\phi_{1,2}^+$ satisfy the GPE. Note that, the collision matrix is still unitary ($|a_g|^2 + |b_g|^2 = 1$), but this is due to the fact that V is evaluated only at time t and position \mathbf{r} , i.e. it is treated as a constant in the integration of the rhs of Eq. (6.2). In particular, the nonlinearity is evaluated only at the previous time step t , without any further iteration so as to preserve unitarity and the consequent unconditional stability [33, 34].

7 Imaginary-time quantum lattice Boltzmann model

The qLB-model has been recently used to compute the ground state solution of the GPE Eq. (6.4) [21]. In this section, we will revise the derivation of the one-dimensional imaginary-time qLB scheme and its application to the computation of the ground state of the GPE. The extension to the multi-dimensional case follows the same line already discussed for the real-time qLB scheme and for details we refer to the original reference [21].

7.1 The time-independent Gross-Pitaevskii equation

In order to find stationary solutions of Eq. (6.4), one usually sets $\psi(\mathbf{r}, t) = \exp(-i\mu t/\hbar)\phi(\mathbf{r})$, where μ is the chemical potential [33, 35]. By inserting the above wave

function into Eq. (6.4), the following equation for μ and $\phi(\mathbf{r})$ is derived

$$\mu\phi(\mathbf{r}) = \left(-\frac{\hbar^2}{2m}\Delta_{\mathbf{r}} + V_{ext}(\mathbf{r}) + NU_d|\phi(\mathbf{r})|^2 \right) \phi(\mathbf{r}), \quad (7.1)$$

with the normalization condition

$$\int_{\mathbb{R}^d} |\phi(\mathbf{r})|^2 = 1.$$

This is a constrained nonlinear eigenvalue problem, any eigenvalue μ can be computed from its corresponding eigenfunction ϕ , by simply multiplying Eq. (7.1) by $\phi^*(\mathbf{r})$ and integrating over \mathbb{R}^d .

The ground state solution is the eigenfunction $\phi_g(\mathbf{r})$ associated with the minimum eigenvalue μ and satisfying the normalization condition.

Typically, ϕ_g is found by applying a transformation known as Wick rotation, to the time-dependent GPE. This consists of “rotating” the time axis on the complex plane so that it becomes purely imaginary [36–39]. Let us introduce an imaginary variable τ defined as $\tau = it$. Rewriting Eq. (6.4) in terms of τ , we obtain a diffusion equation with an absorption/emission term given by the potential

$$\hbar\partial_{\tau}\psi(\mathbf{r},\tau) = \left(\frac{\hbar^2}{2m}\Delta_{\mathbf{r}} - V_{ext}(\mathbf{r}) - NU_d|\psi(\mathbf{r},\tau)|^2 \right) \psi(\mathbf{r},\tau). \quad (7.2)$$

The problem is reduced to solve Eq. (7.2) under the normalization condition constraint given by Eq. (6.3). In fact, for $\tau \rightarrow +\infty$, the solution of this constrained equation tends to a stationary profile, which turns out to be the ground state wave function of the GPE.

7.2 The one-dimensional imaginary-time qLB scheme

The imaginary-time qLB scheme is obtained by applying the Wick rotation to the Dirac Eq. (6.1) from which qLB starts from. The basic idea is to rewrite the Dirac equation (written in Majorana form) with respect to the imaginary variable $\tau = it$.

In the one-dimensional case, we consider Eq. (6.1) and apply the Wick rotation, to yield:

$$\begin{aligned} \partial_{\tau}u_{1,2} - ic\partial_z u_{1,2} &= -i\omega_c d_{2,1} + gu_{1,2}, \\ \partial_{\tau}d_{1,2} + ic\partial_z d_{1,2} &= i\omega_c u_{2,1} + gd_{1,2}. \end{aligned} \quad (7.3)$$

Now, let $\Delta\tau = i\Delta t$ be the imaginary-time discretization step, while $\Delta z = -ic\Delta\tau = c\Delta t$ is, as usual, the spatial step. Integrating Eq. (7.3) along the characteristics of $u_{1,2}$ and $d_{1,2}$ respectively and approximating the rhs integral with the trapezoidal rule, we obtain

$$\begin{aligned} \hat{u}_{1,2} - u_{1,2} &= -i\frac{\tilde{m}}{2}(d_{2,1} + \hat{d}_{2,1}) + \frac{\tilde{g}}{2}(\hat{u}_{1,2} + u_{1,2}), \\ \hat{d}_{1,2} - d_{1,2} &= i\frac{\tilde{m}}{2}(u_{2,1} + \hat{u}_{2,1}) + \frac{\tilde{g}}{2}(\hat{d}_{1,2} + d_{1,2}), \end{aligned} \quad (7.4)$$

where $\hat{u}_{1,2} = u_{1,2}(z + \Delta z, \tau + \Delta \tau)$, $\hat{d}_{1,2} = d_{1,2}(z - \Delta z, \tau + \Delta \tau)$, $u_{1,2} = u_{1,2}(z, \tau)$, $d_{1,2} = d_{1,2}(z, \tau)$, $\tilde{m} = \omega_c \Delta t$ and $\tilde{g} = g \Delta t$. The system of Eq. (7.4) is algebraically solved for $\hat{u}_{1,2}$ and $\hat{d}_{1,2}$, to yield the following explicit scheme

$$\begin{aligned}\hat{u}_{1,2} &= a_g^i u_{1,2} - b_g^i d_{2,1}, \\ \hat{d}_{1,2} &= a_g^i d_{1,2} + b_g^i u_{2,1},\end{aligned}$$

where

$$a_g^i = \frac{(1 - \tilde{g}/2)(1 + \tilde{g}/2) + \tilde{m}^2/4}{(1 - \tilde{g}/2)^2 - \tilde{m}^2/4}, \quad b_g^i = \frac{i\tilde{m}}{(1 - \tilde{g}/2)^2 - \tilde{m}^2/4}.$$

Note that, g is evaluated at time τ , i.e. there is no iteration over the nonlinearity.

We observe that $|a_g^i|^2 + |b_g^i|^2 \neq 1$, hence the collision matrix is not unitary. This implies that the model does not automatically verify the normalization condition. This is usual for models which compute the ground state solution by solving dynamical equations in fictitious time, such as Eq. (7.2). Hence, the normalization condition must be imposed at each time step by directly re-normalizing the wave function [33, 35, 38].

In analogy with real-time qLB, we introduce the wave functions

$$\phi_{1,2}^\pm = \frac{1}{\sqrt{2}} e^{i\omega_c \tau} (u_{1,2} + i d_{2,1}). \quad (7.5)$$

In [21], the equation governing $\phi_{1,2}^-$ is derived and it is shown, by inspecting its dispersion relation, that $\phi_{1,2}^-$ fulfills Eq. (7.2). In particular, it is shown that the dispersion relation of the equation governing $\phi_{1,2}^-$ coincides with the dispersion relation of Eq. (7.2) apart from an additional mode whose effect is to uniformly amplify $\phi_{1,2}^-$, but the normalization step compensates this anomalous behavior. For the details of this procedure, we refer to the original reference [21]. Here we will revise the simpler free-particle case ($V_{ext} = 0$ and $NU_1 = 0$).

Since $u_{1,2}$ and $d_{1,2}$ fulfill Eq. (7.3), $\phi_{1,2}^\pm$ satisfy the following equations:

$$\partial_\tau \phi_{1,2}^+ - ic \partial_z \phi_{1,2}^- = 0, \quad (7.6)$$

$$\partial_\tau \phi_{1,2}^- - ic \partial_z \phi_{1,2}^+ = 2\omega_c \phi_{1,2}^-. \quad (7.7)$$

By multiplying (7.6) by c and taking the z derivative, multiplying Eq. (7.7) by i and deriving it with respect to τ and then subtracting the resulting equations, we obtain the following governing equation for $\phi_{1,2}^-$

$$\hbar \partial_\tau \phi_{1,2}^- = \frac{\hbar^2}{2m} \partial_z^2 \phi_{1,2}^- + \frac{\hbar^2}{2\omega_c} \partial_\tau^2 \phi_{1,2}^-. \quad (7.8)$$

The second order time derivative term drives an instability which tends to amplify $\phi_{1,2}^-$ while preserving its spatial profile. However, the normalization step tames the effect of

this term. This point is clarified by the study of the dispersion relation we mentioned above. Here, we just want to observe that, for the free-particle case ($V_{ext}=0$ and $NU_d=0$), $\phi_{1,2}^-$ obey a diffusion equation with the correct diffusion coefficient (see Eq. (7.2)).

Note that, in this imaginary-time extension of the model, no adiabatic assumption is needed and it is not required to have “small” potential interaction. As we shall see, in this case the nonlinearity coefficient can be set to much larger values than in the real-time case.

8 Numerical results

In this section, we will present some numerical results for the two-dimensional linear Schrödinger, one- and two-dimensional time-dependent GPE and two-dimensional time-independent GPE.

8.1 Linear Schrödinger equation

For the linear Schrödinger equation, we review some of the two-dimensional results presented in [20]. One-dimensional numerical results can be found in [19].

Let us consider, as initial condition, a minimum uncertainty wave packet

$$\psi_0(z,y) = (2\pi\Delta_{0z}\Delta_{0y})^{-1/2} \exp\left(-\frac{(z-z_0)^2}{4\Delta_{0z}^2}\right) \exp\left(-\frac{(y-y_0)^2}{4\Delta_{0y}^2}\right) \exp(-im(v_z z + v_y y)). \quad (8.1)$$

This is a wave packet centered about (z_0, y_0) with initial spreads Δ_{0z} , Δ_{0y} along z and y respectively and propagating at speed (v_z, v_y) . With this initial condition, the analytical solution of the Schrödinger equation for a free propagating particle is given by [40]:

$$\begin{aligned} \psi_{an}(z,y,t) = & \left[2\pi \left(\Delta_{0z} + \frac{it}{2m\Delta_{0z}} \right) \left(\Delta_{0y} + \frac{it}{2m\Delta_{0y}} \right) \right]^{-1/2} \exp\left(-\frac{(z-z_0-v_z t)^2}{4\Delta_{0z}^2 + 2it/m}\right) \\ & \times \exp\left(-\frac{(y-y_0-v_y t)^2}{4\Delta_{0y}^2 + 2it/m}\right) \exp(im(v_z z + v_y y)) \exp\left(-\frac{im(v_z^2 + v_y^2)t}{2}\right). \end{aligned} \quad (8.2)$$

Based on this solution, the mean position $(Z(t), Y(t))$ and the mean spreads $\Delta_z(t)$ and $\Delta_y(t)$ evolve according to the equations

$$Z(t) = z_0 + v_z t, \quad Y(t) = y_0 + v_y t, \quad (8.3)$$

and

$$\Delta_z(t) = \left[\Delta_{0z}^2 + \frac{t^2}{4m^2\Delta_{0z}^2} \right]^{1/2}, \quad \Delta_y(t) = \left[\Delta_{0y}^2 + \frac{t^2}{4m^2\Delta_{0y}^2} \right]^{1/2}. \quad (8.4)$$

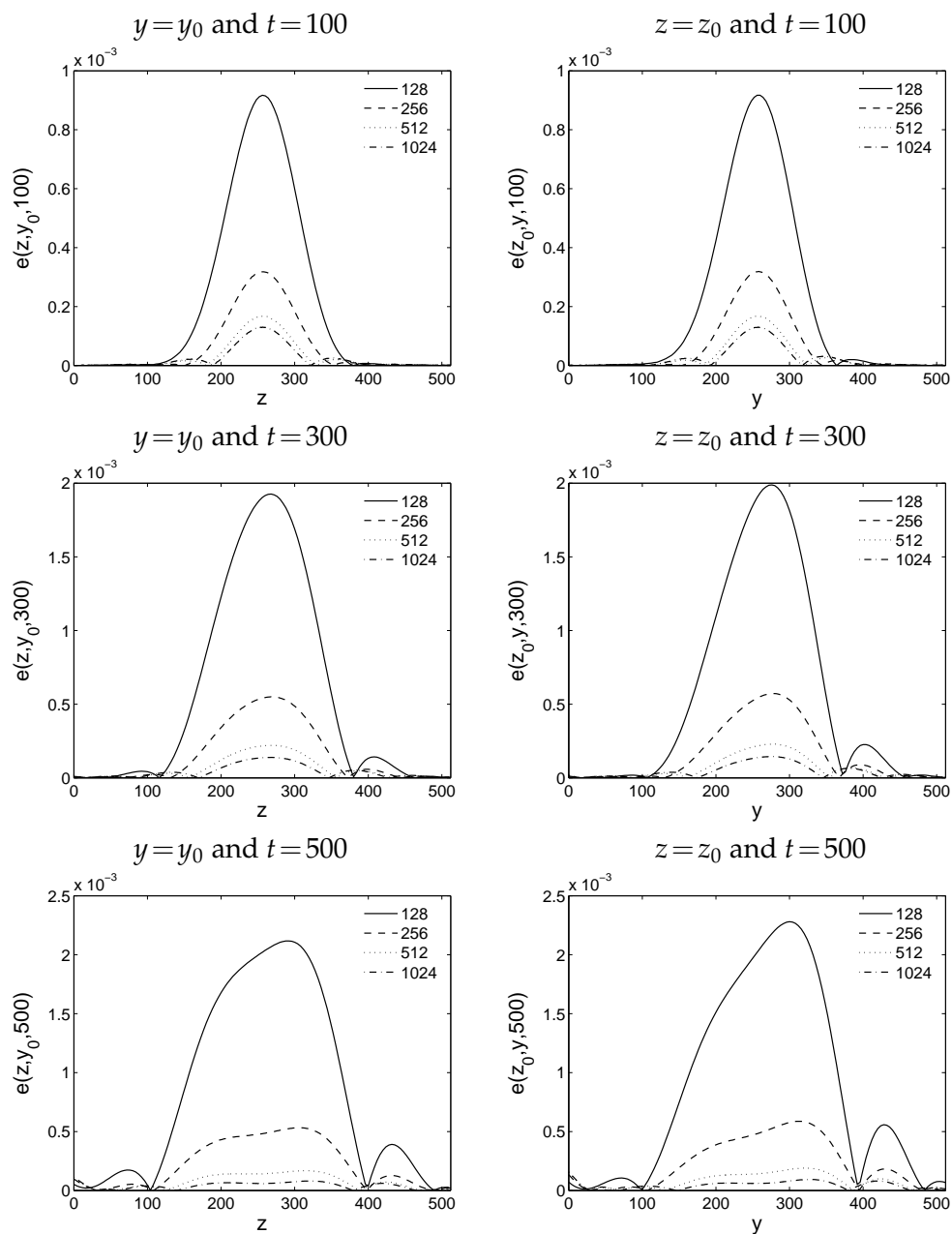


Figure 1: Difference between the real part of the analytical solution and the model result for $y=y_0$ (left column) and $z=z_0$ (right column) (see Eq. (8.5)) and for different values of $N_z=N_y$ at times $t=100$, $t=300$ and $t=500$. Parameters are set as follows: $v_z=0.02$, $v_y=0.04$, $\Delta_{0z}=\Delta_{0y}=40$ and $\tilde{m}=(1/8)h$. Solid line: $N_z=N_y=128$; Dashed line: $N_z=N_y=256$; Dotted line: $N_z=N_y=512$; Dash-dotted line: $N_z=N_y=1024$. Time and space are expressed in lattice units.

We compare the qLB numerical results with the analytical solution while decreasing the discretization step $h \equiv \Delta t = \Delta z = \Delta y$ (recall that $c = 1$ in lattice units). For this numerical test, we set the computational domain as $[0, 512] \times [0, 512]$ and $y_0 = z_0 = 256$ in lattice units and the domain is discretized with $N_z = N_y = 128, 256, 512$ and 1024 lattice points. The remaining parameters are set as follows: $\Delta_{0z} = \Delta_{0y} = 40$, $v_z = 0.02$, $v_y = 0.04$ and $\tilde{m} \equiv \omega_c \Delta t = (1/8)h$. Periodic boundary conditions are imposed in all the simulations. The error with respect to the analytical solution Eq. (8.2) is computed in L^2 norm and is found to decrease from 0.08 to 0.009 as the grid resolution was increased from 128 to 1024 points, but with no clear evidence of a specific convergence rate. This could be the effect of concurrence error sources: the time discretization error ($\mathcal{O}(h^2)$), the splitting error ($\mathcal{O}(h)$) and the lack of adiabaticity for $\tilde{m} = \omega_c \Delta t \rightarrow 0$. In Fig. 1 the function

$$e(z, y, t) = |\Re(\psi_{an}(z, y, t)) - \Re(\phi^+(z, y, t))| \quad (8.5)$$

taken at the cross sections $y = y_0$ and $z = z_0$ for the different values of N_z and N_y is plotted at times 100, 300 and 500.

In Table 1 the propagation velocity and the mean spread of the packet with increasing resolution are also shown. For the present setting the expected velocity is $v_z = 0.02$ and $v_y = 0.04$ and the spread at time $t = 500$ is computed by Eq. (8.4) and is 64.03 since $\Delta_{0z} = \Delta_{0y} = 40$.

Table 1: Propagation velocity and spread of the packet at time $t = 500$ for different values of $N_z = N_y$. The expected values are: $v_z = 0.02$, $v_y = 0.04$ and $\Delta_z(500) = \Delta_y(500) = 64.03$. Here $\tilde{m} = (1/8)h$ and $\Delta_{0z} = \Delta_{0y} = 40$.

$N_z = N_y$	v_z	v_y	$\Delta_z(500)$	$\Delta_y(500)$
128	0.0175	0.0355	60.20	60.19
256	0.0189	0.0379	62.41	62.40
512	0.0191	0.0384	62.97	62.95
1024	0.0193	0.0386	63.11	63.09

Now that the convergence of the scheme has been shown, we set $h = 1$ as it is usual in lattice Boltzmann schemes. We want to show the ability of the model to reproduce the mean quantities $Z(t)$, $Y(t)$, $\Delta_z(t)$ and $\Delta_y(t)$ as functions of time following the theoretical relations of Eqs. (8.3), (8.4). In particular, we set $N_z = N_y = 1024$ and $v_z = 0.05$, $v_y = 0.02$, $\Delta_{0z} = 50$, $\Delta_{0y} = 32$ and $\tilde{m} = 0.2$. In Fig. 2, we compare the numerical curve of $Z(t)$, $Y(t)$, $\Delta_z(t)$ and $\Delta_y(t)$ with the analytical functions given by Eqs. (8.3) and (8.4).

As a second example, we consider the introduction of an harmonic oscillator. The harmonic potential is given by

$$V(z, y) = \frac{1}{2} m \omega_0^2 [(z - z_0)^2 + (y - y_0)^2],$$

where we are assuming for simplicity $\omega_z = \omega_y = \omega_0$, not isotropic harmonic potentials are considered in [20]. It is known that, in this case, the mean position satisfy the classical

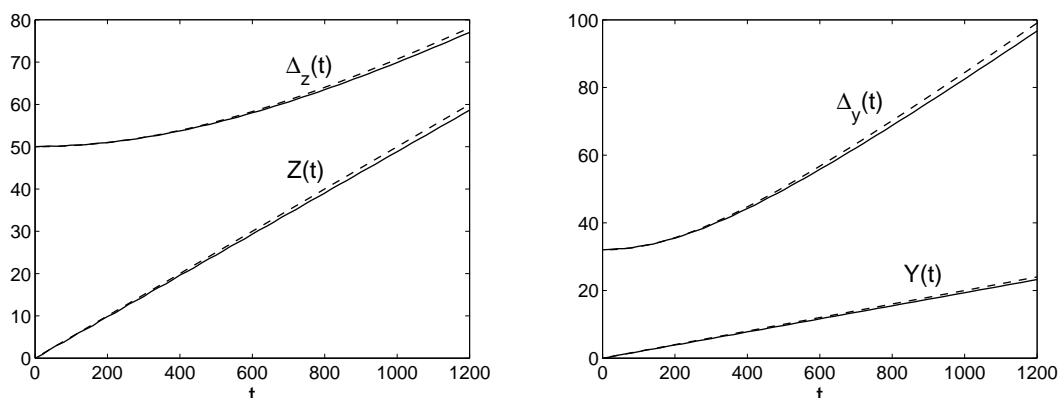


Figure 2: Comparison between $Z(t)$, $Y(t)$, $\Delta_z(t)$ and $\Delta_y(t)$ and the expected curves given by Eqs. (8.3) and (8.4) for the following setting: $N_z = N_y = 1024$, $v_z = 0.05$, $v_y = 0.02$, $\Delta_{0z} = 50$, $\Delta_{0y} = 32$ and $\tilde{m} = 0.2$. Solid lines represent numerical results; dashed lines are the expected curves. Time and space are expressed in lattice units.

equation of motion of the harmonic oscillator and this yields

$$Z(t) = z_0 + \frac{v_z}{\omega_0} \sin(\omega_0 t), \quad Y(t) = y_0 + \frac{v_y}{\omega_0} \sin(\omega_0 t). \quad (8.6)$$

Moreover, by setting $\Delta_0 \equiv \Delta_{0z} = \Delta_{0y}$ so that

$$\omega_0 = \frac{1}{2m\Delta_0^2},$$

the initial spreading is preserved all along the evolution. We want to check the ability of the model to preserve Δ_0 for different parameter settings. In Table 2, the results are shown, here Δ_z and Δ_y are the packet spreads averaged over two periods. In all of the simulations we set $v_z = 0.02$ and $v_y = 0.04$.

Table 2: Averaged variances of the packet along z and y for different setting of the parameters $N_z = N_y$, \tilde{m} and ω_0 . Here $v_z = 0.02$ and $v_y = 0.04$.

$N_z = N_y$	ω_0	\tilde{m}	Δ_z	Δ_y	Expected Δ
1024	$8/64^2$	$1/16$	64.35 ± 1.33	64.35 ± 1.33	64
1024	$2/32^2$	$1/4$	32.25 ± 0.70	32.27 ± 0.75	32
512	$4/32^2$	$1/8$	32.16 ± 0.70	32.17 ± 0.69	32
512	$2/32^2$	$1/4$	31.87 ± 0.27	31.87 ± 0.29	32
512	$1/16^2$	$1/2$	16.01 ± 0.69	16.02 ± 0.70	16
256	$2/16^2$	$1/4$	16.05 ± 0.37	16.05 ± 0.38	16
256	$1/16^2$	$1/2$	15.74 ± 0.32	15.74 ± 0.32	16

In Fig. 3, $Z(t)$, $Y(t)$, $\Delta_z(t)$ and $\Delta_y(t)$ are shown for $N_z = N_y = 512$, $\omega_0 = 2/32^2$, $\tilde{m} = 1/4$.

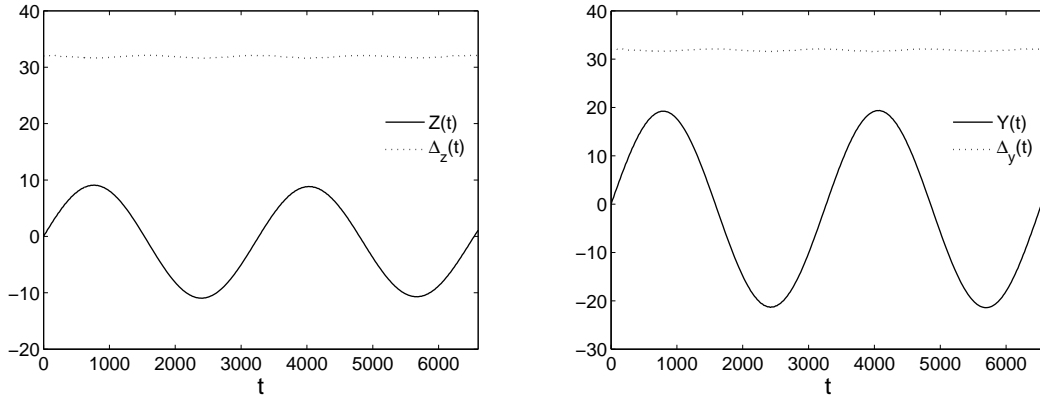


Figure 3: $Z(t)$, $Y(t)$, $\Delta_z(t)$ and $\Delta_y(t)$ for the harmonic oscillator with parameters $N_z = N_y = 512$, $\omega_0 = 2/32^2$, $\tilde{m} = 1/4$, $v_z = 0.02$ and $v_y = 0.04$. The solid lines are $Z(t)$ and $Y(t)$, while the dotted ones are $\Delta_z(t)$ and $\Delta_y(t)$. Time and space are expressed in lattice units.

8.2 Time-dependent GPE

Let us consider the following one-dimensional nonlinear potential

$$V(z, t) = \frac{1}{2} m \omega_0^2 (z - z_0)^2 + V_{nl} |\psi(z, t)|^2,$$

where $V_{nl} \equiv NU_1$. This potential represents a self-interacting particle confined by an harmonic trap. As an initial condition, we use again the one-dimensional Gaussian packet of minimum uncertainty. We compare qLB numerical results with the ones given by a classical Crank-Nicolson (CN) scheme. For both schemes the discretization steps are set as $h \equiv \Delta z = \Delta t = 0.5$ and Dirichlet boundary conditions are imposed.

It is well known that if the number of particles exceeds a given threshold (i.e. the nonlinearity coefficient is larger than a fixed threshold), the BEC becomes unstable. This is due to the fact that, when repulsive forces between the particles of the condensate prevail over the confining effect of the harmonic trap, the BEC droplet breaks up. From a mathematical point of view, this corresponds to the situation where the potential develops a doubly humped structure, so that an initially Gaussian wave packet, representing the BEC droplet, would break up into two or more separate droplets and finally dissolve into a purely chaotic configuration [27].

In one spatial dimension, the critical value, V_c , above which the BEC becomes unstable (expressed in lattice units) is given by

$$V_c = \sqrt{2\pi} \Delta_0^3 \tilde{m} \omega_0^2. \quad (8.7)$$

Let us consider the following set of parameters: $N_z = 512$, $\tilde{m} = 1/4$, $\Delta_0 = 32$ and $\omega_0 = 1/512$. From Eq. (8.7), we obtain $V_c = 0.19625$.

The effect of the nonlinear term is to cyclically contract and expand the wave packet. The amplitude of these contractions/expansions is proportional to the strength of the nonlinear term (i.e. to the value of V_{nl}). However, the condensate remains confined by the harmonic trap.

For $V_{nl} > V_c$, after a large number of time steps, this cyclic behavior is broken and a transition occurs which corresponds to strong variation of the wave function and leads to a chaotic behavior, ending with the total dispersion of the wave packet.

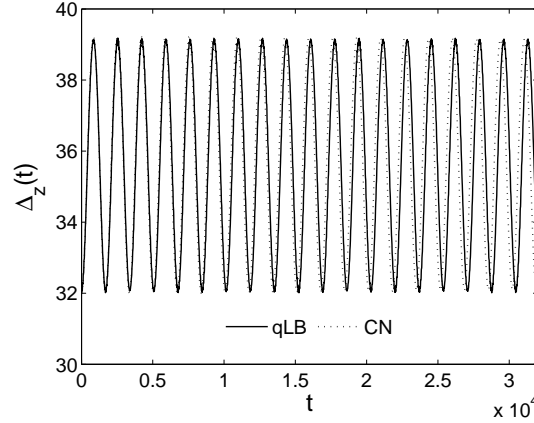


Figure 4: Mean spreading $\Delta_z(t)$ for qLB and CN. Parameters are set as follows: $N_z = 512$, $z_0 = 256$, $\tilde{m} = 1/4$, $\Delta_0 = 32$, $\omega_0 = 1/512$, $v_z = 0.0$, $V_{nl} = 0.1$.

We initially set $V_{nl} = 0.1 < V_c$. In Fig. 4, the mean spreading produced by the two schemes up to time $t = 32200$ ($\sim 10T$, where $T = 2\pi/\omega_0$) is reported. From this figure, we note that the packet spreading is oscillating from 32 (which corresponds to the initial value) to about 39.2, with an oscillation period which is given by $T/2$. However, the two schemes compute a slightly different value for ω_0 . In particular, $\omega_{qLB} = 1.926 \times 10^{-3}$, while $\omega_{CN} = 1.951 \times 10^{-3}$, leading to two different periods, $T_{qLB} \sim 3260$ and $T_{CN} \sim 3220$ while the expected value is $T \sim 3217$. We conclude that, qLB is slightly less accurate than CN in computing the oscillation frequency. This is in line with the general observation that qLB is very efficient in achieving a reasonable accuracy (within a few percent), but cannot easily be pushed to high-accuracy because of the lack of adiabaticity in the limit $\omega_c \Delta t \rightarrow 0$. In Fig. 5, the wave function densities computed by qLB and CN at times 0, $T_{qLB}/4$, $T_{qLB}/2$, $3T_{qLB}/4$, T_{qLB} for qLB and 0, $T_{CN}/4$, $T_{CN}/2$, $3T_{CN}/4$, T_{CN} for CN are shown. We note that the expansion/contraction behavior is well visible and the results are in good agreement. In Fig. 6, kinetic, potential and total energies computed by qLB and CN schemes are also shown. A satisfactory energy conservation is achieved for both models and the mean values of the total energy computed by qLB and CN are $E_{qLB} = 1.413 \times 10^{-3}$ and $E_{CN} = 1.417 \times 10^{-3}$.

Let us briefly investigate the transition that occurs for $V_{nl} > V_c$ after a large number of time steps. In particular, we set $V_{nl} = 0.21 > V_c$, leaving unchanged the remaining pa-

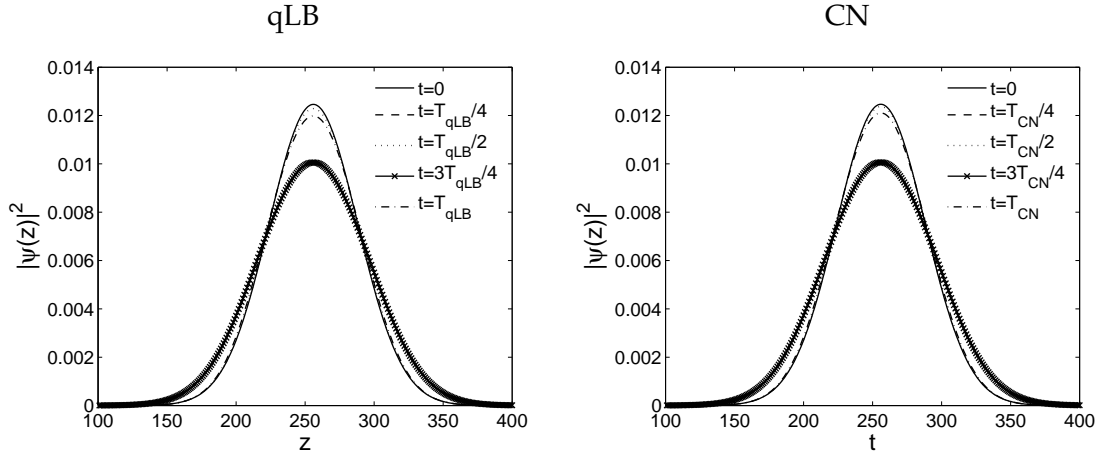


Figure 5: Wave function densities computed by qLB and CN. Parameters are set as follows: $N_z=512$, $z_0=256$, $\tilde{m}=1/4$, $\Delta_0=32$, $\omega_0=1/512$, $v_z=0.0$, $V_{nl}=0.1$. For qLB $|\psi(z,t)|^2$ is computed at times 0 , $T_{qLB}/4$, $T_{qLB}/2$, $3T_{qLB}/4$ and T_{qLB} , while for CN $|\psi(z,t)|^2$ is computed at times 0 , $T_{CN}/4$, $T_{CN}/2$, $3T_{CN}/4$ and T_{CN} .

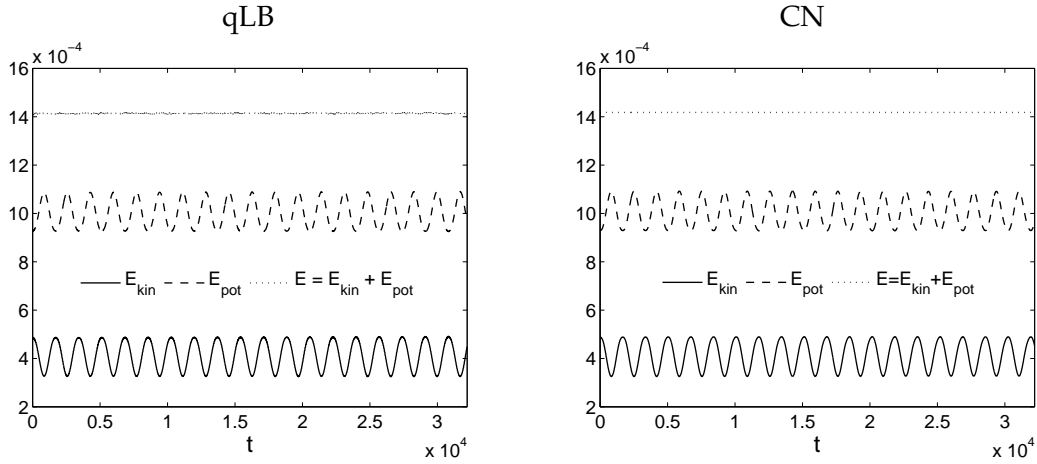


Figure 6: Kinetic, potential and total energy computed by qLB and CN. Parameters are set as follows: $N_z=512$, $z_0=256$, $\tilde{m}=1/4$, $\Delta_0=32$, $\omega_0=1/512$, $v_z=0.0$, $V_{nl}=0.1$.

rameters. After about 98000 time steps ($\sim 30T_{qLB}$), the transition from the cyclic behavior described above to a chaotic state takes place. In Fig. 7, the wave function density computed by qLB at times $30T_{qLB}$, $32T_{qLB}$ and $50T_{qLB}$ is shown.

A similar experiment can be performed in two spatial dimensions. In this case the non-linear potential is given by:

$$V(z,y,t) = \frac{1}{2}m\omega_0^2[(z-z_0)^2 + (y-y_0)^2] + V_{nl}|\psi(z,y,t)|^2,$$

where we are assuming $\omega_0 \equiv \omega_z = \omega_y$.

Using, as an initial condition the wave packet of Eq. (8.1), one can calculate the critical

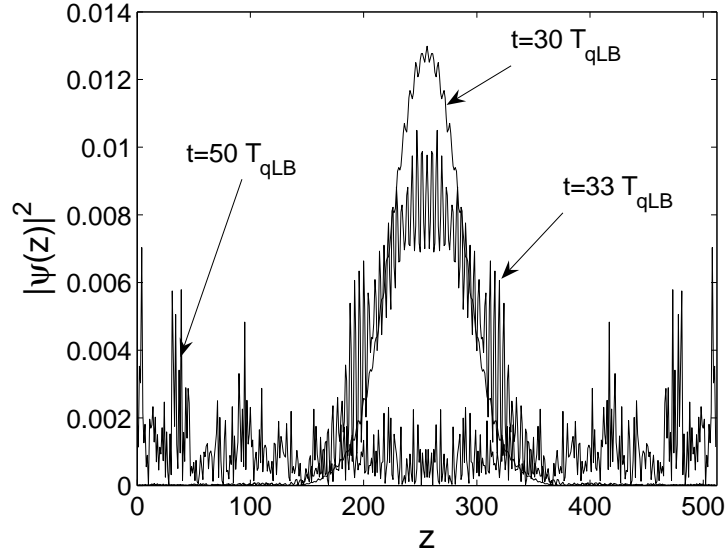


Figure 7: Wave function density computed by qLB when the BEC becomes unstable ($V_{nl} > V_c$). Parameters are set as follows: $N_z = 512$, $z_0 = 256$, $\tilde{m} = 1/4$, $\Delta_0 = 32$, $\omega_0 = 1/512$, $v_z = 0.0$, $V_{nl} = 0.21$. The wave function density is reported at times $30T_{qLB}$, $32T_{qLB}$ and $50T_{qLB}$.

value above which the BEC becomes unstable [27].

In two dimensions, this value is given by:

$$V_c = 2\pi\Delta_0^4\tilde{m}\omega_0^2, \quad (8.8)$$

where all the quantities are expressed in lattice units.

As above, we compare qLB with CN by setting the same discretization step $h \equiv \Delta z = \Delta y = \Delta t = 0.5$ and imposing Dirichlet boundary conditions for both schemes. Moreover, for this simulation, parameters are set as follows: $N_z = N_y = 256$, $\tilde{m} = 1/2$, $\Delta_{0z} = \Delta_{0y} \equiv \Delta_0 = 16$, $\omega_0 = 1/256$, hence, from Eq. (8.8), we obtain $V_c = \pi$.

In this case, we set $V_{nl} = 2\pi > V_c$, and we expect to observe a cyclic behavior for a large number of time steps and then a rapid transition from this stable, oscillating regime to the unstable dispersion of the BEC.

Indeed, for about $100T$, the wave packet contracts and expands itself cyclically, as shown in Fig. 8. In particular, the oscillation frequencies computed by qLB and CN are $\omega_{qLB} = 3.841 \times 10^{-3}$ and $\omega_{CN} = 3.898 \times 10^{-3}$ respectively, leading to the following values for the periods: $T_{qLB} \sim 1635$, $T_{CN} \sim 1611$, while the expected value is $T \sim 1608$. In Fig. 8, the wave function densities taken at $y = y_0$ and computed by qLB and CN at time intervals of a quarter of their periods are shown and they witness a satisfactory agreement.

After about $100T_{qLB}$ time steps, a rapid transition occurs and the wave function starts to break up. In Fig. 9, the unstable behavior of the wave packet is shown, in particular, the wave function density computed by qLB at the cross section $y = y_0$ at times $100T_{qLB}$ and $110T_{qLB}$ is reported.

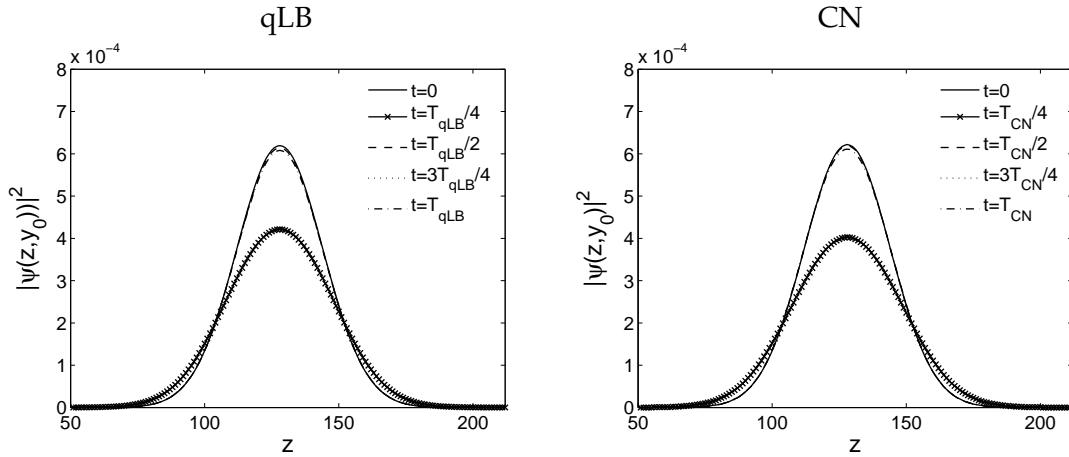


Figure 8: Wave function densities computed by qLB and CN at the cross section $y=y_0$. Parameters are set as follows: $N_z=N_y=256$, $z_0=y_0=128$, $\tilde{m}=1/2$, $\Delta_0=16$, $\omega_0=1/256$, $v_z=v_y=0.0$, $V_{nl}=2\pi$. For qLB $|\psi(z,y,t)|^2$ is computed at times 0 , $T_{qLB}/4$, $T_{qLB}/2$, $3T_{qLB}/4$ and T_{qLB} , while for CN $|\psi(z,y,t)|^2$ is computed at times 0 , $T_{CN}/4$, $T_{CN}/2$, $3T_{CN}/4$ and T_{CN} .

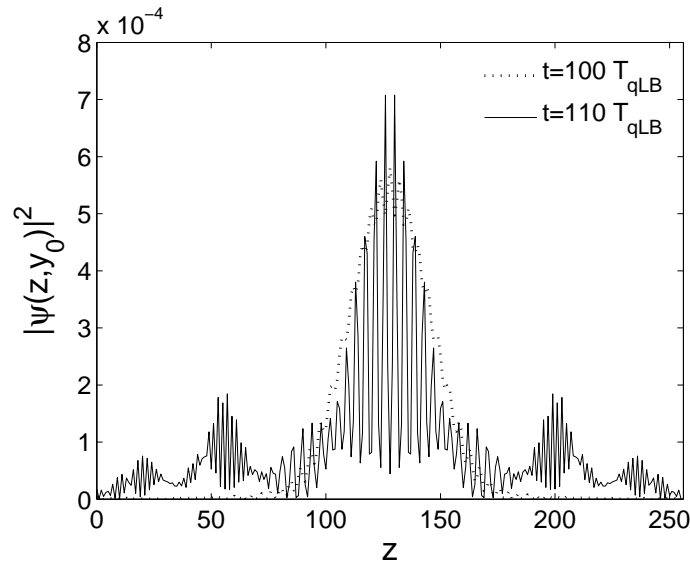


Figure 9: Wave function density computed by qLB when the BEC becomes unstable ($V_{nl} > V_c$). Parameters are set as follows: $N_z N_y = 256$, $z_0 = y_0 = 128$, $\tilde{m} = 1/2$, $\Delta_0 = 16$, $\omega_0 = 1/256$, $v_z = v_y = 0.0$, $V_{nl} = 2\pi$. The wave function density is reported at times $100T_{qLB}$ and $110T_{qLB}$.

8.3 Ground-state computation of the GPE

In this section, we show some numerical results obtained by applying the imaginary-time qLB model to the computation of the ground state of the GPE. Since, qualitatively, one- and two- dimensional results are very similar, we will focus only on two-dimensional

Table 3: Ground state chemical potential μ and maximum value reached by the ground state wave function $\phi_g^0 \equiv \phi_g(x_0, y_0)$ for qLB, CN and BEFD models. Numerical results are also compared with the Thomas-Fermi chemical potential (see Eq. (8.10)). The results are computed for different values of V_{nl} . Parameters are set as follows: $\omega_z = \omega_y = 1/128$, $\tilde{m} = 1/8$, $\Delta_{0z} = \Delta_{0y} = 16$, $N_z = N_y = 512$.

V_{nl}	μ qLB	μ CN	μ BEFD	μ TF	ϕ_g^0 qLB	ϕ_g^0 CN	ϕ_g^0 BEFD
0	0.007816	0.007812	0.007812	–	0.01723	0.01763	0.01763
10	0.009219	0.009250	0.009250	0.004928	0.01627	0.01656	0.01656
100	0.017489	0.017597	0.017597	0.015584	0.01218	0.01226	0.01225
500	0.035802	0.035949	0.035949	0.034846	0.00835	0.00837	0.00836
1000	0.049964	0.050125	0.050125	0.049280	0.00702	0.00704	0.00703
2000	0.070161	0.070338	0.070338	0.069692	0.00590	0.00591	0.00591
3000	0.085721	0.085905	0.085905	0.085355	0.00533	0.00534	0.00534
4000	0.098860	0.099050	0.099050	0.098560	0.00496	0.00497	0.00496
5000	0.110447	0.110642	0.110642	0.110193	0.00469	0.00470	0.00470
10000	0.155967	0.156176	0.156176	0.155837	0.00395	0.00395	0.00395

simulations. For details on one-dimensional numerical results, we refer the reader to the original work [21].

In order to validate our numerical results, we compare qLB with classical Crank-Nicholson scheme and with a backward Euler finite difference (BEFD) scheme [21,33]. We also use, as a second term of comparison, the analytic solution obtained in the Thomas-Fermi limit. This approximation is valid in the strong-interaction limit, in which kinetic energy contributions can be neglected [41]. This limit is reached for large values of the non-linearity coupling constant NU_d .

By considering the time-independent GPE of Eq. (7.1) and neglecting the kinetic energy term, we obtain

$$\mu_{TF}\phi(\mathbf{r}) = (V_{ext}(\mathbf{r}) + NU_d|\phi(\mathbf{r})|^2)\phi(\mathbf{r}),$$

where we indicate μ with μ_{TF} to recall that this is the Thomas-Fermi chemical potential.

In this case the solution is trivial and the wave function density is given by

$$|\phi(\mathbf{r})|^2 = \frac{1}{NU_d}(\mu_{TF} - V_{ext}(\mathbf{r}))\Theta(\mu_{TF} - V_{ext}(\mathbf{r})), \quad (8.9)$$

where Θ is the Heaviside step function. The chemical potential given by this approximation, μ_{TF} , can be computed by directly imposing the normalization condition to the wave function density of Eq. (8.9). In the two-dimensional case, we obtain

$$\mu_{TF} = \left(NU_2 \frac{m\omega_0^2}{\pi} \right)^{1/2}. \quad (8.10)$$

Let us consider the following two-dimensional nonlinear potential

$$V(z, y, \tau) = \frac{1}{2}m\omega_0^2[(z - z_0)^2 + (y - y_0)^2] + V_{nl}|\phi(z, t, \tau)|^2,$$

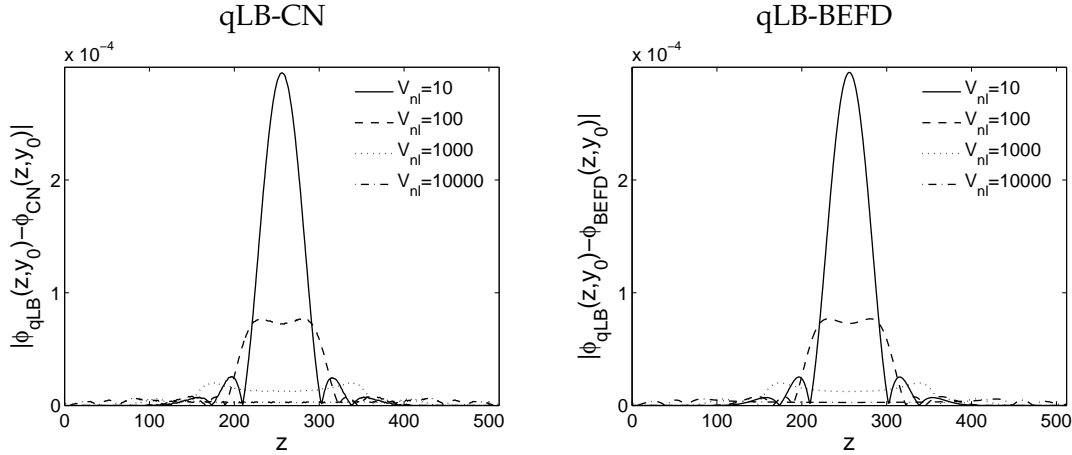


Figure 10: Deviations of qLB from CN and BEFD in the computation of the ground state wave function for different values of V_{nl} . In particular, $|(\phi_g)_{qLB}(z, y_0) - (\phi_g)_{CN}(z, y_0)|$ and $|(\phi_g)_{qLB}(z, y_0) - (\phi_g)_{BEFD}(z, y_0)|$ computed at the qLB nodal are plotted. Simulation parameters are set as: $\tilde{m}=1/8$, $\Delta_{0z}=\Delta_{0y}=16$, $\omega_0=1/128$, $N_z=N_y=512$. Space is expressed in lattice units.

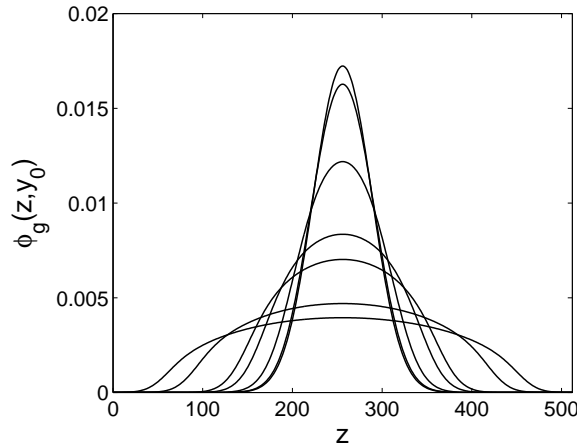


Figure 11: Ground state profiles given by the qLB model for different values of V_{nl} . Simulation parameters are set as: $\tilde{m}=1/8$, $\Delta_{0z}=\Delta_{0y}=16$, $\omega_0=1/128$, $N_z=N_y=512$. V_{nl} takes the following values: 0, 10, 100, 500, 1000, 5000 and 10000 (top to bottom). Space is expressed in lattice units.

where $V_{nl} = NU_2$ and τ is the fictitious time variable introduced in Section 7. As initial condition, the wave packet of Eq. (8.1) is again used and Dirichlet boundary conditions are imposed for all the three schemes.

Let $[0, 512] \times [0, 512]$ be our numerical domain (expressed in lattice units) and the remaining parameters are set as follows: $\Delta_{0z} = \Delta_{0y} = 16$, $\omega_0 = 1/128$ and $\tilde{m} = 1/8$. Discretization steps for qLB are set to unity, while for CN and BEFD we set $\Delta_z = \Delta_y = 0.5$ and $\Delta t = 0.1$. The simulation must be stopped only when a stationary state is reached, hence

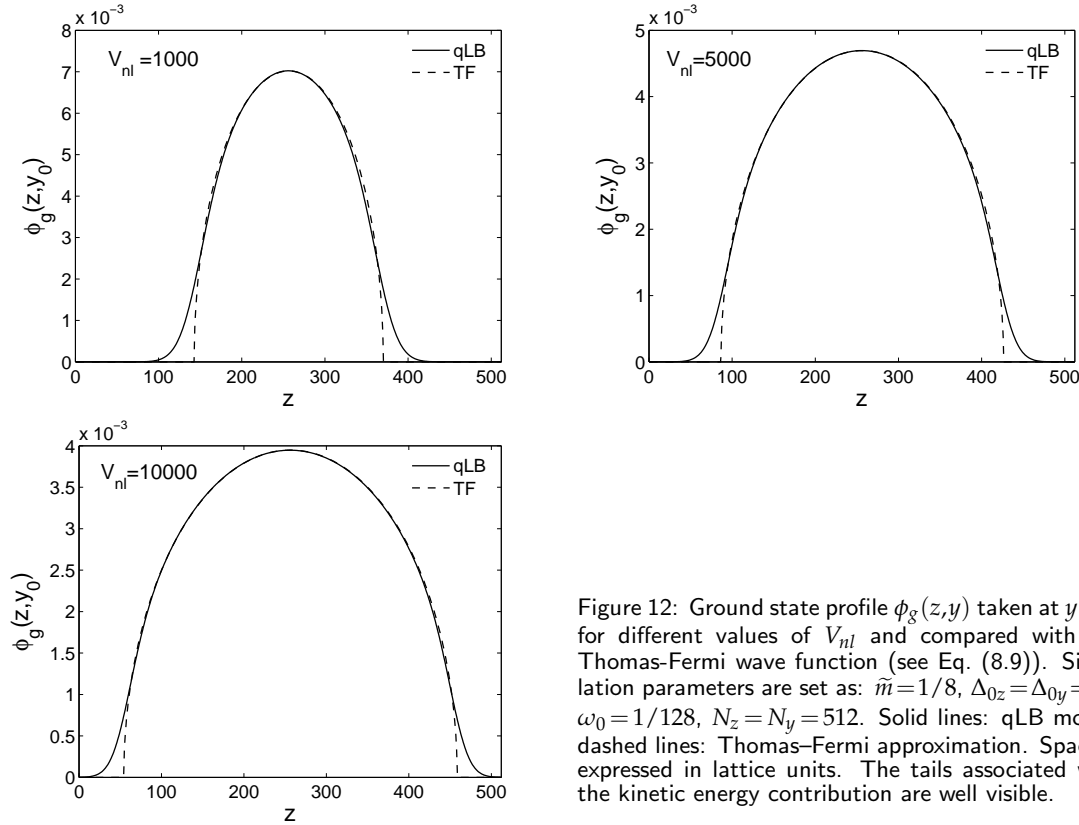


Figure 12: Ground state profile $\phi_g(z, y)$ taken at $y=y_0$ for different values of V_{nl} and compared with the Thomas-Fermi wave function (see Eq. (8.9)). Simulation parameters are set as: $\tilde{m}=1/8$, $\Delta_{0z}=\Delta_{0y}=16$, $\omega_0=1/128$, $N_z=N_y=512$. Solid lines: qLB model; dashed lines: Thomas-Fermi approximation. Space is expressed in lattice units. The tails associated with the kinetic energy contribution are well visible.

the following stop criterion is imposed

$$\max_{i,j=0,\dots,N_g} |\phi_{ij}^{n+1} - \phi_{ij}^n| < \varepsilon,$$

where N_g is the number of nodal point and $\varepsilon=10^{-9}$.

In Table 3, the limit value of μ and the maximum value of ϕ at the end of the simulation, $(\phi_g(z_0, y_0))$, are reported for the three schemes. Moreover, the Thomas-Fermi chemical potential μ_{TF} given by Eq. (8.10) is also shown. In Fig. 10, we compare the ground state wave function $\phi_g(z, y)$ taken at $y=y_0$ computed by qLB with the profiles given by CN and BEFD. In particular, in the figure we report the deviations between qLB and CN or BEFD: $|(\phi_g)_{qLB}(z, y_0) - (\phi_g)_{CN}(z, y_0)|$ and $|(\phi_g)_{qLB}(z, y_0) - (\phi_g)_{BEFD}(z, y_0)|$ computed at the qLB nodal points. In Fig. 11, $\phi_g(z, y)$ taken at $y=y_0$ and computed by qLB for different values of V_{nl} is reported to show the qualitative effect of an increasing nonlinearity coefficient. Finally, in Fig. 12, we compare qLB results with the wave function given by the Thomas-Fermi approximation of Eq. (8.9) for some values of V_{nl} . The tail smoothing, well visible in the qLB results, is due to the kinetic energy contribution, hence, it is not reproduced by the Thomas-Fermi approximation where the kinetic term is neglected.

These data witness a satisfactory agreement between qLB and the reference CN and

BEFD solutions, while CN and BEFD are in excellent agreement with each other (this is due to the higher resolution adopted in these reference cases).

9 Conclusions and outlook

In this work, we have reviewed the derivation of the quantum lattice Boltzmann model and its most recent developments. In particular, we have shown the viability of the qLB scheme for the numerical solution of the time-dependent Schrödinger equation, as well as its non-linear extension, such as the Gross-Pitaevskii equation for Bose-Einstein condensates, in multiple spatial dimensions. Moreover, the formulation of an imaginary-time qLB model for the ground-state computation of the GPE has also been reviewed.

Being based on a unitary, first-order, relativistic formulation, at variance with most explicit schemes for non-relativistic quantum wave equations, the qLB method offers unconditional stability with the size of the time-step/mesh-size. In addition, being based on a first-order, hyperbolic formulation, stability can be preserved with a time-step scaling linearly with the mesh size, rather than quadratically like most explicit schemes for quantum wave equations [34].

However, its accuracy is subject to the condition $\omega_c \Delta t = \Delta x / \lambda_B \leq 1$, $\lambda_B = c / \omega_c$ being the De Broglie wavelength of the particle. Since the time-step scales linearly with the mesh-spacing (a result of the relativistic formulation), qLB can be taken down to very refined grids without suffering the time-step collapse typical of non-relativistic Courant-Friedrichs-Lewy stability conditions, $\Delta t < 2m\Delta x^2 / \hbar$, thus compensating for its low-order accuracy. However, care must be taken to ensure that errors due to lack of adiabaticity remain under control when $\omega_c \Delta t$ is sent to zero.

The qLB method is also very interesting as a prospective algorithm for quantum computers [8, 11, 13–15]. Indeed, as observed in [42], the stream-and-collide structure of the quantum lattice Boltzmann equation maps naturally onto the structure of quantum networks, i.e. quantum computing devices consisting of quantum logic gates, whose computational operation proceeds synchronously in time. In these networks, the output of some gates are wire-connected to the input of some others (streaming step), and locally processed by unitary operations (the collision step).

Besides this attractive, but still speculative application, qLB is an interesting scheme that can be easily implemented in classical (electronic) computers. As an explicit numerical scheme, qLB offers an appealing set of features, such as unconditioned stability, norm-preserving (unitarity) and amenability to parallel processing.

In conclusion, the qLB method makes an excellent candidate for implementation on classical computers as well as for prospective quantum computing applications.

References

- [1] G. McNamara and G. Zanetti, Use of the Boltzmann equation to simulate lattice-gas automata, *Phys. Rev. Lett.*, 61 (1988), 2332–2335.

- [2] F. Higuera and J. Jimenez, Boltzmann approach to lattice gas simulations, *Europhys. Lett.*, 9 (1989), 663–668.
- [3] F. Higuera, S. Succi and R. Benzi, Lattice gas dynamics with enhanced collisions, *Europhys. Lett.*, 9 (1989), 345–349.
- [4] R. Benzi, S. Succi and M. Vergassola, The lattice Boltzmann equation: theory and applications, *Phys. Rep.*, 222 (1992), 145–197.
- [5] J. L. Lebowitz, S. Orszag and Y. Qian (eds.), *J. Stat. Phys.*, Special issue on Lattice models, 81 (1995).
- [6] I. V. Karlin, S. Ansumali, C. E. Frouzakis and S. S. Chikatamarla, Elements of the lattice Boltzmann method I: Linear advection equation, *Commun. Comput. Phys.*, 1 (2006), 616–655.
- [7] I. V. Karlin, S. S. Chikatamarla and S. Ansumali, Elements of the lattice Boltzmann method II: Kinetics and hydrodynamics in one dimension. *Commun. Comput. Phys.*, 2 (2007), 196–238.
- [8] B. M. Boghosian and W. Taylor, Simulating quantum mechanics on a quantum computer, *Physica D*, 120 (1998), 30–42.
- [9] B. M. Boghosian and W. Taylor, Quantum lattice-gas model for the many-particle Schrödinger equation in d dimensions, *Physical Review E*, 57 (1998), 54–66.
- [10] I. Bialynicki-Birula, Weyl, Dirac, and Maxwell equations on a lattice as unitary cellular automata, *Physical Review D*, 49 (1994), 6920–6927.
- [11] D. A. Meyer, From quantum cellular automata to quantum lattice gases, *J. Stat. Phys.*, 85 (1996), 551–574.
- [12] D. A. Meyer, Quantum lattice gases and their invariants, *Int. J. Mod. Phys. C*, 8 (1997), 717–735.
- [13] J. Yepez, Quantum computation for physical modeling, *Comput. Phys. Commun.*, 146 (2002), 277–279.
- [14] J. Yepez, Quantum lattice-gas model for computational fluid dynamics, *Phys. Rev. E*, 63 (2001), 046702.
- [15] G. Vahala, L. Vahala and J. Yepez, Quantum lattice gas representation of some classical solitons, *Phys. Lett. A*, 310 (2003), 187–196.
- [16] S. Succi and R. Benzi, Lattice Boltzmann equation for quantum mechanics, *Physica D*, 69 (1993), 327–332.
- [17] R. Feynman, Simulating Physics with computers, *Int. J. Theoret. Phys.*, 21 (1982), 467–488.
- [18] D. P. di Vincenzo, Quantum computation, *Science*, 270 (1995), 255–261.
- [19] S. Succi, Numerical solution of the Schrödinger equation using discrete kinetic theory, *Phys. Rev. E*, 53 (1996), 1969–1975.
- [20] S. Palpacelli and S. Succi, Numerical validation of the quantum lattice Boltzmann scheme in two and three dimensions, *Phys. Rev. E.*, 75 (2007), 066704.
- [21] S. Palpacelli, S. Succi and R. Spigler, Ground-state computation of Bose-Einstein condensates by an imaginary-time quantum lattice Boltzmann scheme, *Phys. Rev. E*, 76 (2007), 036712.
- [22] S. Succi, Lattice Boltzmann schemes for quantum applications, *Comp. Phys. Comm.*, 146 (2002), 317–323.
- [23] E. Madelung, Quantum theory in hydrodynamical form, *Z. Phys.*, 40 (1926), 332–336.
- [24] L. Landau, E. Lifshitz, *Relativistic Quantum Field Theory*, (Pergamon, Oxford, 1960).
- [25] S. Succi, Lattice Boltzmann equation for relativistic quantum mechanics, *Phil. Trans. R. Soc. Lond. A*, 360 (2002), 429–436.
- [26] L. I. Schiff, *Quantum Mechanics*, 3rd edition McGraw-Hill, New York (1968).
- [27] S. Succi, Lattice quantum mechanics: an application to Bose-Einstein condensation, *Int. J.*

- Mod. Phys. C, 9 (1998), 1577–1585.
- [28] A. Griffin, D. Snoko and S. Stringari (eds.), Bose-Einstein Condensation (Cambridge Univ. Press, New York, 1995).
 - [29] A. D. Jackson, G. M. Kavoulakis and C. J. Pethick, Solitary waves in clouds of Bose-Einstein condensed atoms, Phys. Rev. A, 58 (1998), 2417–2422.
 - [30] P. Leboeuf and N. Pavloff, Bose-Einstein beams: Coherent propagation through a guide, Phys. Rev. A, 64 (2001), 033602.
 - [31] W. Bao and W. Tang, Ground state solution of Bose-Einstein condensate by directly minimizing the energy functional, J. Comput. Phys., 187 (2003), 230–254.
 - [32] S. K. Adhikari, Numerical study of the spherically symmetric Gross-Pitaevskii equation in two space dimensions, Phys. Rev. E, 62 (2000), 2937–2944.
 - [33] W. Bao and Q. Du, Computing the ground state solution of Bose-Einstein condensates by a normalized gradient flow, SIAM J. Sci. Comput., 25 (2004), 1674–1697.
 - [34] K. C. Kulander (ed.), Time-Dependent Methods for Quantum Dynamics, thematic issue, Comp. Phys. Commun. 63, (North-Holland, Amsterdam, 1991).
 - [35] W. Bao, Chern and F. Y. Lim, Efficient and spectrally accurate numerical methods for computing ground and first excited states in Bose-Einstein condensates, J. Comput. Phys., 219 (2006), 836–854.
 - [36] A. Aftalion and Q. Du, Vortices in a rotating Bose-Einstein condensate: Critical angular velocities and energy diagrams in the Thomas-Fermi regime, Phys. Rev. A, 64 (2001), 063603.
 - [37] M. M. Cerimele, M. L. Chiofalo, F. Pistella, S. Succi and M. P. Tosi, Numerical solution of the Gross-Pitaevskii equation using an explicit finite-difference scheme, Phys. Rev. E, 62 (2000), 1382–1389.
 - [38] M. L. Chiofalo, S. Succi and M. P. Tosi, Ground state of trapped interacting Bose-Einstein condensates by an explicit imaginary-time algorithm, Phys. Rev. E, 62 (2000), 7438-7444.
 - [39] A. Minguzzi, S. Succi, F. Toschi, M. P. Tosi and P. Vignolo, Numerical methods for atomic quantum gases with applications to Bose-Einstein condensates and to ultracold fermions, Phys. Rep., 395 (2004), 223–355.
 - [40] S. Gasiorowicz, Quantum Physics (Wiley, New York, 1974).
 - [41] F. Dalfovo, L. Pitaevskii and S. Stringari, The condensate wave function of a trapped atomic gas, J. Res. Natl. Inst. Stand. Technol., 101 (1996), 537–544.
 - [42] P. Love and B. Boghosian, Type II quantum algorithms, Physica A, 362 (2006), 210–214.